

Two-phase Transport Properties and Transport Simulation of the Gas Diffusion Layer of a PEFC

Tetsuya Koido, Toru Furusawa, Koji Moriyama, and Keiichiro Takato
Fundamental Research Center, Honda R&D, Co. Ltd., 1-4-1 Chuo, Wako-shi, Saitama,
351-0193, Japan

A series of analysis methods is proposed to simulate the liquid gas two-phase and multi-component transport phenomena in the gas diffusion layer (GDL) of a polymer electrolyte fuel cell (PEFC). These methods involve measuring and predicting the two-phase flow properties of a GDL, the capillary pressure and relative permeability, and simulating the two-phase multi-component transport in the GDL. The methods are described and applied to a carbon-fiber paper GDL. The predicted two-phase flow properties correctly captured the shape of the curve of the measured results and showed the similar magnitude to those. Transport simulation is carried out with the properties to identify in detail the two-phase multi-component transport. Since the fibrous structure and wettability of the GDL are considered, advanced analysis can be conducted with the methods.

Introduction

Since the GDL of a PEFC is usually made of electrically conductive and opaque material such as carbon fiber, it is hard to visualize or measure the liquid condition, phase velocity, and species concentration in the GDL. Various simulation efforts have been tried to elucidate the two-phase transport phenomena in the GDL (1-9). Darcy's law has been applied in the literature to simulate two-phase flow in a GDL with properties involving the two-phase effect.

In general, the capillary pressure and relative permeability are regarded as the dominant properties of the gas-liquid two-phase flow characteristics in a porous medium (10). Liquid water is driven by capillary pressure which is defined as the difference between the gas and liquid phase pressures as

$$P_c = P_g - P_l. \quad [1]$$

As the liquid phase pressure changes with the void space occupied by liquid water, the capillary pressure depends on the liquid saturation, s , which is defined as the liquid volume fraction of the total pore space in the porous medium as

$$s = V_l / V_{pore}. \quad [2]$$

The relative permeability of each phase is defined as the ratio of the permeability of the phase at a given saturation level to the absolute permeability of the porous medium as described in Eq. 3.

$$u_g = \frac{Kk_{rg}}{\mu_g L} \Delta P_g \quad , \quad u_l = \frac{Kk_{rl}}{\mu_l L} \Delta P_l \quad [3]$$

Although a fundamental understanding of two-phase flow in a GDL is of great importance in analyzing the effect of the flooding phenomenon on the PEFC performance, studies on two-phase flow properties measurement for a GDL used in a fuel cell are limited (11-13). As an alternative approach, the properties have been empirically derived from lithological experiments (1,10,14-16).

The simulations presented in refs. 1-9 have been attempted with those properties from porous media other than an actual GDL as stated above or with an estimated value from indirect measurements. It is therefore desirable to identify a method that can elucidate the phenomena in GDL resulting from the effects of such properties as the fibrous structure and wettability.

Measurement and Prediction Methods

This present study uses a carbon-fiber paper as the GDL material that has been treated with a 5% by wt. solution of poly-tetra-fluoro-ethylene (PTFE) because a GDL is commonly a porous medium whose porosity is high enough for gas transport and with wettability that is highly hydrophobic for easy drainage of liquid water. Fundamental properties of the GDL were obtained by general measurement methods: the contact angle, porosity, pore size distribution, and absolute permeability were respectively measured by the Wilhelmy or droplet method, pycnometer method, mercury porosimetry, and capillary flow porosimetry (17).

The following subsections describe a series of analysis methods to elucidate the transport phenomena in a GDL. These methods involve measuring the two-phase flow properties of a GDL, predicting those properties, and simulating the two-phase multi-species transport in a GDL.

Capillary Pressure

Measurement. Figure 1 shows a schematic diagram of a device for measuring the capillary pressure *versus* saturation (P_c - s) curve that is based on the porous diaphragm method (10, 18). The GDL disk sample is placed inside the chamber, and liquid water is forced into the porous sample from below by air pressure. After the steady state has been attained, the capillary pressure and saturation are respectively measured from the liquid water pressure and the amount of water contained in the pore space of the sample. The P_c - s imbibition curve is determined by repeating this procedure in small increments at each steady state until liquid water penetrates the GDL. The gas phase pressure in the calculation of capillary pressure is assumed to be the atmospheric pressure. The saturation is determined by precisely measuring the mass of liquid water forced into the GDL sample and calculating the ratio of the liquid water volume converted from this liquid water mass to the total pore volume.

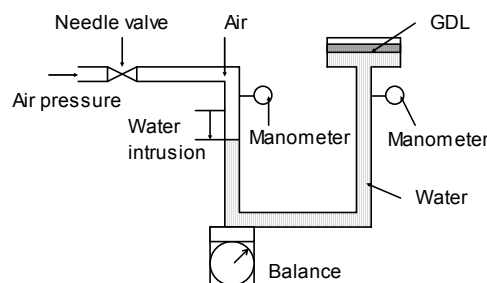


Figure 1. Schematic diagram of the device for measurement of the P_c - s curve.

Prediction. We applied pore network model (19, 20) to predict the P_c - s curve of the GDL. The model idealizes the pore morphology and topology as a pore network consisting of pores and throats. The pore network can be constructed based with the pore size distribution of the GDL measured by the mercury porosimetry and the connectivity number. The connectivity number is extracted by applying an image processing technique that employs the thinning algorithm (21, 22) to the image that has been obtained by the microfocal X-ray CT of the carbon paper. Figure 2 shows the image of the GDL which consists of non-woven carbon fibers each with a diameter of about $7\mu\text{m}$ and the respective porosity is 0.79. It also shows the result of applying the thinning algorithm. The gray objects in Figure 2 show the fibrous structure of the GDL, and the distributed dots show the skeleton of the pore network, which means the flow paths in the GDL. The connectivity number is calculated by counting the average number of skeleton lines at each connection point.

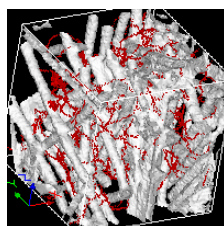


Figure 2. Skeleton of pore network in the microfocal X-ray CT image of the GDL.

Applying the Young-Laplace law as in Eq. 4 to the pore network enables the P_c - s curve to be calculated. The contact angle, pore curvature which is based on the pore size distribution, and surface tension of water are used in this equation. Water is forced from the inlet to outlet of this pore network according to Eq. 4. Calculation parameters are described in Table I. The contact angle is measured by the Wilhelmy method.

$$P_c = 2\sigma \cos \theta_c / r \quad [4]$$

TABLE I. Calculation parameters for the pore network model.

Contact angle, θ_c	Surface tension, σ	Connectivity number, N
162°	$70.25 \cdot 10^{-3} \text{ N/m}$	4.9

Relative Permeability

Measurement. Various measurements of relative permeability have been conducted by the steady-state test method for reservoir rock, sand stone, and other porous media

(23-25). We also used the steady state method to measure the relative permeability of the gas phase.

A schematic drawing of the test apparatus is shown in Figure 3. The GDL test piece is sandwiched between similar GDLs on the inlet and outlet sides. The GDL on the inlet side ensures homogeneous distribution of liquid water in the planar direction, while the one on the outlet side minimizes the effect of the outflow boundary. Liquid is injected first and then a constant flow rate of air is established. The pressure difference is measured after the pressure has stabilized. The GDL test piece is removed immediately after the pressure measurement so that the weight can be measured to deduce the saturation. The measured pressure difference, air flow rate, and saturation are combined as in Eq. 3 with the absolute permeability measured by capillary flow porosimetry to derive the relative permeability of the gas phase.

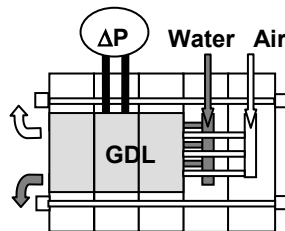


Figure 3. Schematic diagram of the device for measuring the relative permeability.

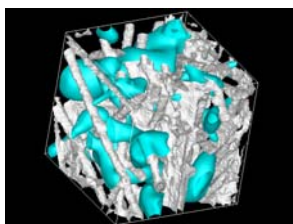
Prediction. The two-phase lattice Boltzmann method (TLBM) can be a useful tool for studying the complex behavior of two-phase flow such as coalescence and the breakup of water in a porous medium with Young-Laplace law (26). Although it is possible to simulate the arbitrary contact angle and capillary number of a water droplet by applying TLBM to GDL, it is difficult to represent the real properties of liquid water and air at the same time in complex geometry (27). Such properties include the viscosity, density, and surface tension. To resolve this problem, we propose a method that combines TLBM described in refs. 26, 27, 28 and 29 and the single-phase lattice Boltzmann method (SLBM) described in ref. 30 to predict the relative permeability of GDL. The proposed relative permeability prediction method is described by the following steps.

- Step 1: Reconstructing a voxel image of a GDL from microfocal X-ray slice images.
- Step 2: Calculating the absolute permeability of the voxel image by the SLBM approach. Details of the conditions are shown in Table II. Inlet velocity is set as $7.0 \cdot 10^{-4}$ m/s.
- Step 3: Calculating the two phase flow by the TLBM approach. Details of the conditions are also shown in Table II, and the periodic boundary condition is applied. We could then obtain the water distribution in the GDL at a certain saturation level.
- Step 4: Calculating the permeability for the water distribution obtained in Step 3 by the SLBM approach. Liquid water and fibers are regarded as solid in this step. The relative permeability of the gas phase (k_{rg}) can then be obtained by calculating the ratio between this permeability and the absolute permeability calculated in Step 1.
- Step 5: Performing similar calculation for the relative permeability of the liquid phase (k_{rl}). The gas phase and fibers are regarded as solid in this step.

Figure 4 shows the fibrous structure and water distribution in GDL (Step 3).

TABLE II. Calculation conditions for LBM

Property	Value for SLBM (Steps 2, 4, and 5)	Value for TLBM (non-dimensional; Step 3)
Velocity model	D3Q15 model	D3Q15 model
Calculation domain, $L_x \cdot L_y \cdot L_z$	122·122·122 μm	122·122·122
Density of gas, ρ_g	1.0 kg/m^3	80
Density of liquid, ρ_l	1000 kg/m^3	160
Viscosity of gas, μ_g	$21 \cdot 10^{-6} \text{ Pa}\cdot\text{s}$	$1.6 \cdot 10^{-4}$
Viscosity of liquid, μ_l	$370 \cdot 10^{-6} \text{ Pa}\cdot\text{s}$	$5.01 \cdot 10^{-4}$
Contact angle, θ_c	-	135°
Surface tension, σ	-	18.92
Body force, g_b	-	0.001
Green's function regarding the surface tension, g_s	-	0.001
Green's function regarding wettability of gas, g_g	-	-0.025
Green's function regarding wettability of liquid, g_l	-	0.025

Figure 4. Fibrous structure and water distribution in GDL with the TLBM approach ($s=0.216$).

Transport Simulation

The multi-phase mixture model developed by Wang *et al.* (14) is applied in this study to simulate the two-phase flow and species transport in GDL. This model solves a set of macroscopic equations for multi-phase multi-component flow in a porous medium. It employs Darcy's law for each phase as described in Eq. 3, and assumes interfacial thermal and chemical equilibrium between the phases. The saturation, which is calculated by the liquid water concentration, affects the capillary pressure, relative permeability, and diffusion coefficient of species in the gas phase in this model.

The equations in this study are arranged for an isothermal immiscible two-phase system involving a liquid water phase and gas phase which consists of oxygen, water vapor, and nitrogen. They can be arranged in a simple mathematical form that is suitable for numerical simulation. The formulation basically follows that in ref. 3. and it is implemented in a 3-D numerical solver of advection diffusion equations based on the finite volume method described in ref. 31.

A steady state 1-D computation was carried out for a cathode GDL with boundary conditions for water generation and oxygen consumption corresponding to current density I at one end ($x = 0$) and a fixed pressure, species concentration, and liquid saturation at the other end ($x = L$). The physical properties, dimensions, and boundary conditions are summarized in Table III. It should be noted that the liquid phase pressure at the gas channel end ($x = L$) is set by adding the capillary pressure at the saturation to the gas phase pressure. The absolute permeability is measured by the capillary flow porosimetry. Values for the oxygen diffusion coefficient, liquid water viscosity, liquid water density, and gas viscosity were taken from the literature (2), and the computational region is divided into 100 equally spaced control volumes. The applied two-phase transport properties, capillary pressure and relative permeability are described in the Results and Discussion section.

TABLE III. Physical properties, dimensions, and boundary conditions.

Property	Value
GDL thickness, L	200 μm
GDL porosity, ϵ	0.8
GDL absolute permeability, K	$9 \cdot 10^{-12} \text{ m}^2$
Saturated water vapor concentration, $C_{sat}^{H_2O}$	16.1 mol/m ³
Temperature, T	80°C
Net water transport coefficient, α	0.5
Gas pressure at $x=L$, $P_g _{x=L}$	202650 Pa
Oxygen concentration at $x=L$, $C_g^{O_2} _{x=L}$	11.2 mol/m ³
Saturation at $x=L$, $s _{x=L}$	0.2
Current density, I	20000 A/m ²

Results and Discussion

Capillary pressure

Figure 5 shows a comparison of the measured results for the carbon-fiber paper GDL with the calculated results. The experiments were repeatedly performed on carbon-fiber paper samples that had been treated with 5% by wt. of PTFE. The repeated experiments showed similar of P_c - s curves, although some variation occurred due to the difficulty in measuring the small liquid saturation. A typical result is shown in Figure 5. The calculation was performed by using a pore network model with the GDL properties.

It can be seen from the comparison that the calculated data are similar to the measured data in magnitude, shape and breakthrough point of the P_c - s curve. The curve near the breakthrough point has a gentle slope, indicating that the liquid water could easily intrude when the capillary pressure reached nearly the breakthrough point. Since the majority of pores in the GDL are concentrated in the vicinity of the peak size pore from the mercury porosimetry data, this corresponds to the breakthrough capillary pressure.

The calculation method was therefore successful in expressing a P_c - s curve using the GDL properties, thus leading to a physical interpretation of the relationships between the GDL properties and the curve. Furthermore, the simulation method is able to predict the P_c - s curve for GDLs of various different properties such as wettability, pore size distribution, and pore connectivity, without needing actual samples.

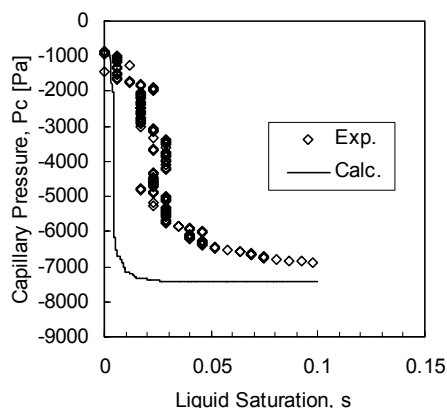


Figure 5. Comparison of the measured capillary pressure with the calculated data.

Relative Permeability

A comparison between the calculated and the experimental data is presented in Figure 6. GDL treated with 5% by wt. of PTFE was used for this experiment and calculation. Static contact angle θ_c , which was measured by the droplet method, was used in this simulation (Table II), because dynamic contact angles such as advancing and receding contact angles can be spontaneously represented by the TLBM approach. The relative permeability of the liquid phase near $s = 0$ and of the gas phase near $s = 1$ could not be predicted by this simulation; this was because the paths of the liquid phase in the GDL were not connected from the inlet to outlet at a low saturation level and the paths of the gas phase were not connected from the inlet to outlet at a high saturation level.

The predicted relative permeability of gas phase correctly captured the shape of the curve of the measured results and showed the similar magnitude to those at a low saturation level. We therefore assumed that the prediction method can be applied to the relative permeability of liquid phase successfully.

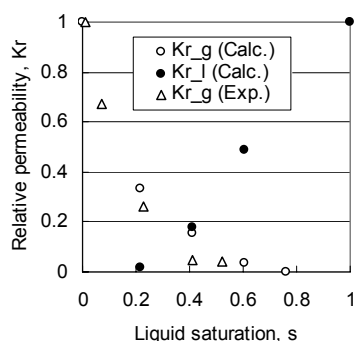


Figure 6. Comparison of the measured relative permeability with the calculated data.

Transport Simulation

The constitutive equations for capillary pressure and relative permeability were modeled by correlating with the measured capillary pressure data (Figure 5) and measured relative permeability of the gas phase (Figure 6), and with the predicted relative permeability of the liquid phase (Figure 6). These correlated models were then applied to a numerical computation. It should be noted that the liquid saturation is defined in the measurement and the prediction as the ratio of the total liquid water volume to the total pore volume in a porous medium although liquid water may be unevenly distributed. On the other hand, the liquid saturation in the transport simulation is considered as the ratio of the local average liquid water volume to the local average pore volume. It is also important to note that the capillary pressure could not be measured or predicted above a liquid saturation level of about 0.1 and the relative permeability of the liquid phase could not be predicted under a liquid saturation level of 0.2 as described in the previous section. In order that these parameters can be applied to the macroscopic approach, we have extrapolated the data in Figures 5 and 6 to fit the constitutive equations.

Figure 7 shows the computational results for the species concentration and liquid saturation. The liquid saturation is high at the catalyst layer end ($x = 0$) due to water generation, while the oxygen concentration is low due to consumption. The water vapor concentration is constant because isothermal condition is assumed.

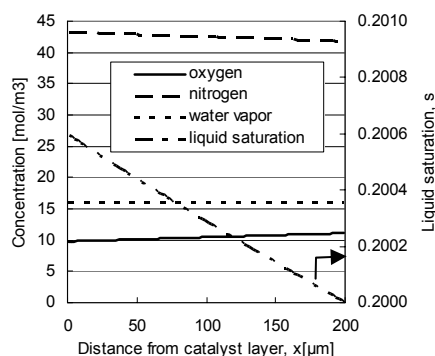


Figure 7. Distribution of the species concentration and liquid saturation

The mass flux and intrinsic local mass average velocity (32) were extracted from the computational result at the middle point ($x = L/2$) to identify in detail the transport phenomenon in the GDL with the result summarized in Table IV. It shows that the gas phase mass flux is negative and that it flows from the gas channel end to the catalyst layer end, in contrast to the liquid phase that flows from the catalyst layer end to the gas channel end. Oxygen moves much faster than the gas phase velocity because diffusion due to the concentration gradient is large. Water vapor moves at the same velocity as the gas phase mixture velocity because of the uniform concentration due to isothermal assumption. Although nitrogen does not move in the macroscopic sense, the diffusion velocity, which is the difference between the velocity of the species and the gas phase velocity, is positive. This means that the positive diffusion and negative advection are balanced. Compared to the liquid phase water mass flux, a one digit lower amount of gas phase water is transported in the reverse direction.

Although this transport simulation of the two-phase flow properties of GDL needs to be developed further to incorporate the thermal effect and the effect when coupled with other layers, it does provide insight into the hidden phenomena of a GDL. Experimental validation of the calculated saturation is also desirable.

TABLE IV. Mass flux and velocity in GDL at $x = L/2$.

Substance		Mass flux [$\text{kg}/(\text{m}^2\text{s})$]	Intrinsic velocity [m/s]
Gas phase	Mixture	$\rho_g u_g = -1.67 \cdot 10^{-3}$	$u_{\text{Int},g} = -1.44 \cdot 10^{-3}$
	O_2	$n_g^{O_2} = -1.66 \cdot 10^{-3}$	$u_{\text{Int},g}^{O_2} = -7.73 \cdot 10^{-3}$
	H_2O	$n_g^{H_2O} = -2.67 \cdot 10^{-4}$	$u_{\text{Int},g}^{H_2O} = -1.44 \cdot 10^{-3}$
	N_2	$n_g^{N_2} = 0$	$u_{\text{Int},g}^{N_2} = 0$
Liquid phase (water)		$\rho_l u_l = 3.75 \cdot 10^{-3}$	$u_{\text{Int},l} = 2.40 \cdot 10^{-5}$

Conclusions

We have proposed a series of methods to analyze the transport phenomena involved in liquid-gas two-phase multi-component flow in the GDL of a PEFC. These methods were applied to measure the capillary pressure and relative permeability of the gas phase of an actual carbon-fiber paper GDL, to predict the capillary pressure and relative permeability for both phases of the GDL, and to simulate two-phase multi-component flow in the GDL. Since the fibrous structure and wettability of the GDL are considered in the methods, advanced analysis can be conducted.

The predicted capillary pressure and relative permeability correctly captured the shape of the curve of the measured results and showed the similar magnitude to those.

Transport simulation was carried out with the properties to identify in detail the two-phase multi-component transport in GDL.

Acknowledgments

The authors wish to thank C. Y. Wang for helping us to understand the multi-phase mixture model in detail.

References

1. U. Pasaogullari and C. Y. Wang, *J. Electrochem. Soc.*, **151**, A399-A406 (2004).
2. U. Pasaogullari and C. Y. Wang, *Electrochimica Acta*, **49**, 4359-4369 (2004).
3. U. Pasaogullari and C. Y. Wang, *J. Electrochem. Soc.*, **152**, A380-A390 (2005).
4. U. Pasaogullari, C. Y. Wang, and K. S. Chen, *J. Electrochem. Soc.*, **152**, A1574-A1582 (2005).
5. H. Meng and C. Y. Wang, *J. Electrochem. Soc.*, **152**, A1733-A1741 (2005).
6. G. Lin, W. He and T. V. Nguyen, *J. Electrochem. Soc.*, **151**, A1999-A2006 (2004).
7. T. V. Nguyen and W. He, in *Handbook of Fuel Cells-Fundamentals, Technology and Applications*, W. Vielstich, A. Lamm, and H. A. Gasteiger, Editors, Vol. 3, p. 325, John Wiley & Sons (2003).
8. G. Lin and T. V. Nguyen, *J. Electrochem. Soc.*, **153**, A372-A382 (2006).
9. J. H. Nam and M. Kaviani, *Int. J. Heat Mass Transfer*, **46**, 4595-4611 (2003).
10. F. A. L. Dullien, *Porous Media: Fluid Transport and Pore Structure, Second Edition*, Academic Press (1992).
11. D. Natarajan and T. V. Nguyen, *J. Electrochem. Soc.*, **148**, A1324 (2001).
12. J. T. Gostick, M. W. Fowler, M. A. Ioannidis, M. D. Pritzker, Y. M. Volfkovich, and A. Sakars, *J. Power Sources*, **156**, 375-387 (2006).
13. H. Ohn and T. Nguyen, Proton Exchange Membrane Fuel Cells V, Electrochemical Society Meeting, Los Angeles, CA, Paper # 1013, Oct. 16-21 (2005).
14. C. Y. Wang and P. Cheng, *Adv. Heat Transfer*, **30**, 93, Academic Press (1997).
15. C.Y. Wang, *Numerical Heat Transfer B, Fundam.*, **31**, 85 (1997).
16. M. Kaviani, in *Principles of Heat Transfer in Porous Media, Second Edition*, Springer, New York (1999).
17. M. F. Mathias, J. Roth, J. Fleming and W. Lehnert, in *Handbook of Fuel Cells-Fundamentals, Technology and Applications*, W. Lietsich, A. Lamm, and H. A. Gasteiger, Editors, Vol.3, Part3, p.517, John Wiley & Sons (2003).
18. F. A. L. Dullien, C. Zarcone, I. F. Macdonald, A. Collins, and R. D. E. Bochard, *J. Colloid and Interface Science*, **127**(2), 362 (1989).
19. S. Bekke and P. E. Oren, *SPE Journal*, **2**, 136-149 (1997).
20. R. G. Hughes and M. J. Blunt, *Advances in Water Resources*, **24**, 409-421 (2001).
21. J. Toriwaki, *Three Dimensional Digital Image Processing*, Shokoudo Press, Japan (2002).
22. W. B. Lindquist, *Journal of Geophysical Research*, **101**, B4, 8297-8310 (1996).
23. J. G. Richardson, J. K. Kerver, J. A. Hafford, and J. S. Osoba, *Petroleum Transactions, AIME*, **195**, 187 (1952).
24. F. G. McCaffery and D. W. Bennion, *J. Canadian Petroleum Tech.*, **13**, 42 (1974).
25. E. Dana and F. Skoczylas, *Int. J. Multiphase Flow*, **28**, 1719-1736 (2002).
26. H. Li, C. Pan and C. T. Miller, *Physical Review E*, **72** (2005).
27. C. Pan, M. Hilpert and C. T. Miller, *Water Resources Research*, **40** (2004).

28. X. Shan and H. Chen, *Physical Review E*, **47**, Number 3 (1993).
29. X. Shan and H. Chen, *Physical Review E*, **49**, Number 4 (1994).
30. Y. H. Qian, D. d'Humieres, and P. Lallemand, *Europhys. Lett.*, **17** (1992).
31. S. V. Patankar, *Numerical Heat Transfer and Fluid Flow*, Hemisphere (1980).
32. R. B. Bird, W. E. Stewart, and E. N. Lightfoot, *Transport Phenomena*, John Wiley & Sons (1960).

Nomenclature

C	molar concentration, mol/m ³
D	mass diffusivity of species, m ² /s
g_g	Green's function regarding interaction between a solid and gas
g_l	Green's function regarding interaction between a solid and liquid
g_s	Green's function regarding interaction between a gas and liquid
g_b	Body force, non-dimensional
I	current density, A/ m ²
K	permeability, m ²
k_r	relative permeability
L	length, m
M	molecule weight, kg/mol
n	mass flux, kg/(m ² s)
N	connectivity number
P	pressure, Pa
r	pore curvature, m
s	saturation of liquid water
T	temperature, K, °C
u	velocity, m/s
V	volume, m ³
x, y, z	in direction x, y, z

Greek symbols

α	net water molar flux per proton molar flux through a PEM
ρ	density, kg/m ³
μ	viscosity, kg/m s
θ_c	contact angle, °
ε	porosity
σ	surface tension force, N/m or non-dimensional

Superscripts and Subscripts

c	capillary
g	gas phase
H_2O	water
Int	intrinsic
l	liquid
N_2	nitrogen
O_2	oxygen
$pore$	pore in a porous medium
sat	saturated value